CHEMISTRY OF MATERIALS

Open Access

pubs.acs.org/cm

Article

Charge Evolution in the $Y_{0.9}Ba_{1.7}Ca_{2.4}Fe_5O_{14.7}$ Layered Perovskite

Published as part of Chemistry of Materials virtual special issue "C. N. R. Rao at 90".

Xabier Martínez de Irujo-Labalde, Masato Goto, Esteban Urones-Garrote, Ulises Amador, Clemens Ritter, Midori Amano-Patino, Yuichi Shimakawa,* and Susana García-Martín*

Cite This: *Chem. Mater.* 2024, 36, 5184–5191

Read Online

ACCESS | Metrics & More | Article Recommendations | Supporting Information

ABSTRACT: The A mixed-valence $Y_{0.9}Ba_{1.7}Ca_{2.4}Fe_5O_{14.7}$ layered perovskite is obtained after topochemical oxygen insertion in $Y_{0.9}Ba_{1.7}Ca_{2.4}Fe_5O_{13}$ under ozone flow. The crystal structure has been determined with a combination of diffraction and microscopy techniques. Mössbauer spectroscopy reveals a 5 $Fe^{3.8+} \rightarrow 2\ Fe^{3+} + 3\ Fe^{(4+\delta)+}$ charge disproportionation accompanied by a smooth magnetic and electronic transition beginning at about 125 K. A layered arrangement of Fe^{3+} and $Fe^{(4+\delta)+}$ assisted by the layered character of the crystal structure is suggested. Two-dimensional magnetic interactions are detected from the magnetic behavior of the oxide and neutron diffraction experiments.

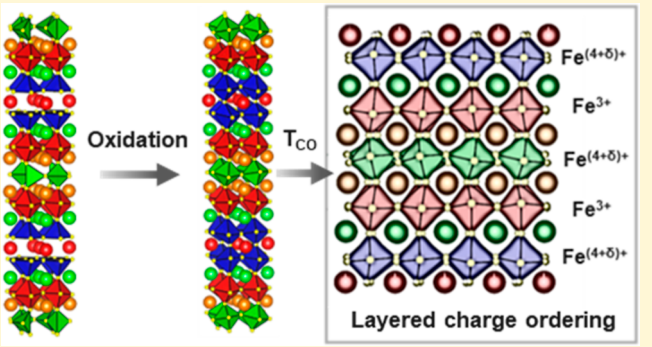

INTRODUCTION

Transition metal (TM) oxides with perovskite related structures have been crucial systems to establish fundamental solid-state chemistry concepts for understanding the functionality of relevant materials.[1] In the perovskite structure, with ABO_3 stoichiometry, the TM atoms occupy the B-sites in an oxygen octahedral coordination environment. The B−O bonding, which highly depends on the nature of the TM, determines the electronic structure of the oxide. In addition to the nature of the "B^{n+} cation", the increase of the formal n+ valence state leads to an increase of the covalency of the B−O bonding. However, the electronic instability of the high-valent cations is often relieved either by charge transfer ($d^n \rightarrow d^{n+1}L$, where L represents a hole in the 2p orbital of the anion) that creates holes in the oxygen band or by charge disproportionation (CD) ($2M^{n+} \rightarrow M^{(n-\delta)} + M^{(n+\delta)}$). CD can undergo a charge ordering (CO) transition accompanied by a change of properties, as it happens in the Verwey transition of Fe_3O_4, with a drastic drop in the electrical resistivity above the transition temperature (T = 125 K).[2] Metal-to-insulator transitions in TM oxides are accompanied by huge resistivity changes, as in the high-temperature superconducting cuprates, but near the transition temperature, the metallic state shows spin, charge, and orbital orderings, which are not proper of ordinary metals.[3] These different electronic structures and the potential transitions from itinerant to localized electronic behavior govern a wide range of properties in perovskite oxides with functionalities for the modern most avant-garde technological applications. For instance, the so-called lattice oxygen redox chemistry (LOM) mechanism, taking place in perovskite oxides with electron transfer from oxygen ligands to TM cations, has been recognized as responsible for the oxygen evolution reaction of some oxygen electrodes for electrolyzers,[4] while colossal magnetoresistance in perovskites is associated with CO effects.[5]

Perovskite oxides with Fe in a high-valent 4+ formal oxidation state are unparalleled frameworks to achieve novel CO patterns with potential impact on the electric and/or magnetic properties.[6,7] The electronic stability of Fe^{4+} is closely related to the arrangement of oxygen around Fe. In $SrFeO_3$, the high hybridization of the Fe 3d and O 2p orbitals avoids the Jahn−Teller distortion to take place as well as the localization of the electrons, which explains the metallic conduction of the oxide.[8,9] However, Fe^{4+} in $CaFeO_3$ is electronically unstable below 290 K and undergoes a CD into Fe^{3+} and Fe^{5+} ($2Fe^{4+}2Fe^{4+} \rightarrow Fe^{3+} + Fe^{5+}$) that order in a rock-salt manner.[10,11] The bending of the O−Fe−O angle in $CaFeO_3$, in contrast with the linear bonding in the $SrFeO_3$, narrows the conduction band, destabilizing the metallic state and facilitating the CO-semiconducting behavior. Metal-to-insulator transition, accompanied by structural accommodation, results from the gradual substitution of Sr^{2+} by Ca^{2+} in the $Sr_{1-x}Ca_xFeO_3$ system.[12] In addition to the size, the oxidation

Received: February 27, 2024
Revised: April 30, 2024
Accepted: May 1, 2024
Published: May 10, 2024

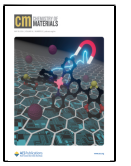

state of the A-cations can play an important role in the CO model, as it happens in the $La_xCa_{1-x}FeO_3$ system, where the substitution of Ca by La modifies the charge disproportionated $Fe^{3+\delta}/Fe^{5-\delta}$ ratio.[13] An interesting interplay between cation ordering and CO is found in some layered perovskites. An excellent example is $YBaFe_2O_5$. The different sizes of Y and Ba drive their ordering into alternate layers in such a way that the Ba atoms present 12 oxygen coordinations, while the Y atoms are eight-coordinated because all the Fe atoms are in square pyramidal coordination and have a 2.5 + average oxidation state. Below 308 K, the mixed-valent (MV) $YBaFe_2O_5$ undergoes a CO transition with Fe^{2+} and Fe^{3+} ordered in chains within the plane due to the presence of orbital ordering, instead of adopting the more stable rock salt-type of CO.[14] In the case of oxides of high-valent Fe, another peculiar type of CO associated with the A-cation ordering is found in the above-mentioned $La_xCa_{1-x}FeO_3$system, where the ordering between La^{3+} and Ca^{2+} in the 3-fold layer-ordered $LaCa_2Fe_3O_9$ forces $Fe^{3.67+}$ to disproportionate into Fe^{5+} and Fe^{3+} in a 1:2 ratio with layered CO extended in the range between 230 and 170 K. This CO implies a great impact on the magnetic properties since a bidimensional helical magnetic ordering takes place only for the Fe^{3+} cations.[15,16] The stabilization of the layered CO in $LaCa_2Fe_3O_9$, although in a narrow range of temperatures, gives some clues in the search for other candidates offering nonrock-salt CO patterns. In $LaCa_2Fe_3O_9$, the rock salt ordering becomes again more stable below 170 K as the three-dimensional (3D) electrostatic lattice energy overcomes the two-dimensional (2D) layered electrostatic potential at the ground state. Therefore, the CD of noninteger high-valent Fe into non-1:1 ratios of Fe^{5+} and Fe^{3+} might be planned taking into account the 3D electrostatic lattice energy and making the CO pattern susceptible to other driving forces such as the layered A-cation ordering. In this context, the mixed-valence $Fe^{3,5+}$ in the layered-ordered double perovskite $SmBaFe_2O_6$ relieves its electronic instability through cascade charge transitions. The first CO transition leads to Fe^{3+}/Fe^{4+}, followed by the CD of the metastable Fe^{4+} into Fe^{3+} and Fe^{5+}. Based on electrostatic lattice energy calculations, a rock-salt-type CO model is proposed for $SmBa(Fe^{3+}Fe^{4+})O_6$, while the CO model for $SmBa(Fe^{3+}_{1.5}Fe^{5+}_{0.5})O_6$ consists of the Fe^{5+} ions surrounded by the Fe^{3+} ions.[17] The complete destabilization of rock-salt-type CO is also achieved in perovskites with Fe^{4+} coexisting with the disproportionated Fe^{5+} and Fe^{3+}. Indeed, the coexistence of Fe^{4+} with Fe^{3+} can be found in $La_{0.3}Sr_{0.7}FeO_3$[18] and $Sr_nFe_nO_{3n-1}$ (n = 4, 8),[19−21] offering CO patterns different than those of the rock-salt type. Furthermore, the coexistence of three oxidation states of Fe seems to be present in the $La_{1-x}Sr_xFeO_3$ (x = 0.6, 0.8) oxides with average valence states $Fe^{3.6+}$ and $Fe^{3.8+}$, where partial CD appears to occur, but the type of CO patterns formed have not been reported so far.[13]

Considering the previous works, our starting point was the idea that stable novel CO patterns could be achieved through more complex layered A-site-ordered perovskite structure oxides, which allow instable noninteger high valence states for Fe to be relieved by inducing partial charge disproportionated states. In this sense, the oxides of the $A_{3m+5n}Fe_{3m+5n}O_{8m+13n}$ homologous series [A = Gd^{3+} (or Tb^{3+}), Ba^{2+}, and Ca^{2+} with m = 1, n = 0; m = 1, n = 1; m = 0, n = 1, respectively] present layer-ordered perovskite-type structures. The RE/Ba/Ca composition highly influences the cation ordering along the c-axis as well as the type and layered ordering of the oxygen polyhedra around the Fe^{3+} cations, which in turn determines their magnetic behavior.[22,23] These oxides of this homologous series present stoichiometric anion sublattices that fix the 3+ oxidation state of the Fe atoms. However, substitution of Gd^{3+} or Tb^{3+} by Y^{3+}, while maintaining the layered-type ordering of cations and Fe-coordination polyhedra, does not preserve the 122 stoichiometry of Y/Ba/Ca, and the anion stoichiometry can more easily be modified by oxidation, thus increasing the Fe-oxidation state. In addition, the nonmagnetic Y does not contribute to the magnetic behavior of the compounds, which can be only related to the Fe atoms. Among this family, we have selected the oxide with composition $Y_{0.9}Ba_{1.7}Ca_{2.4}Fe_5O_{13}$ that presents a complex $10a_p$ layered superstructure (a_p refers to the lattice parameter of the perovskite structure).[24] We report herein the topochemical insertion of oxygen in the compound leading to $Y_{0.9}Ba_{1.7}Ca_{2.4}Fe_5O_{14.7}$ with Fe in the unusual oxidation state of 3.78+. The high instability of $Fe^{3,78+}$ causes disproportion to $Fe^{3+}/Fe^{4+\delta}$. The interplay between the CD transitions, crystal structure, and magnetic behavior is presented.

EXPERIMENTAL METHODS

$Y_{0.9}Ba_{1.7}Ca_{2.4}Fe_5O_{13}$ was prepared by the conventional ceramic method using Y_2O_3 (Aldrich 99.9%), $BaCO_3$ (Aldrich 99.99%), $CaCO_3$ (Merck 99.7%), and Fe_2O_3 (Aldrich 99.99%). Y_2O_3 was dried at 1173 K prior to weighing to avoid $Y(OH)_2$ formation. Stoichiometric amounts of the starting materials were mixed and heated at 1173 K in air to decompose the Ba and Ca carbonates. Afterward, the sample was pelletized and heated at 1473 K in air for 48 h with intermediate grindings. The precursor was then heated at 473 K under flowing ozone-containing oxygen. The initial phase identification and preliminary structural analysis were carried out by powder X-ray diffraction (PXRD) using the Bruker D8 diffractometer.

Transmission electron microscopy (TEM), including high-resolution TEM (HRTEM), selected area electron diffraction (SAED), and electron energy-loss spectroscopy were performed with a JEOL JEM 3000F microscope operating at 300 kV (double tilt ±20°), fitted with an X-ray energy-dispersive spectroscopy (XEDS) microanalysis system (OXFORD INCA) and ENFINA spectrometer with an energy resolution of 1.2 eV. The average oxidation state of Fe cations in the oxide before the ozone oxidation was determined by electron energy loss spectroscopy (EELS).

The spectra were acquired in diffraction mode, with a dispersion of 0.1 eV/channel, a collection angle $\beta \sim 5.4$ mrad, and an acquisition time of 1.5 s. A power-law model was used to remove the background of the spectra.

High-angle annular dark field (HAADF) and annular bright field (ABF) analyses were performed on an ARM200cF microscope fitted with a condensed lens aberration corrector (point resolution in STEM mode of 0.08 nm). HAADF images were acquired with an inner acceptance angle of 90 mrad and ABF images with a collection angle of 11 mrad. The same ARM200cF microscope was employed for EELS mapping since it is fitted with a GIF Quantum-ER spectrometer. EELS mapping was performed with the Y-L2,3 Fe-L2,3, Ba-M4,5, and Ca-L2,3 edge signals, with a collection semiangle $\beta \sim 30$ mrad, a dispersion energy of 0.5 eV/channel, and a collection time for each spectrum of 0.09 s.

Synchrotron X-ray diffraction (SXRD) experiments were carried out at beamline BL01C2 of the Taiwan Light Source, National Synchrotron Radiation Research Center (TLS, NSRRC). Neutron diffraction (ND) data were measured at room temperature (RT) at the Institut Laue Langevin (ILL) in Grenoble, France, using the high-resolution powder diffractometer D2B with λ = 1.594 Å. High-intensity data were taken as a function of temperature between 1.5 and 200 K on the powder diffractometer D20, as well as at the ILL, with λ = 2.41 Å. The crystal structures were refined by the Rietveld method using FullProf.[25]

https://doi.org/10.1021/acs.chemmater.4c00552
Chem. Mater. 2024, 36, 5184−5191

The oxygen content of the oxidized sample was determined by thermogravimetric analysis (TGA) from RT to 1100 °C in a flow of 5% H2−95% Ar mixture with a heating rate of 10 °C min^{-1} using a NETZSCH STA 449 F3.

^{57}Fe Mössbauer spectroscopy measurements were carried out in transmission geometry with a constant acceleration spectrometer using a ^{57}Co/Rh radiation source. The obtained data were fitted with Lorentzian functions. Data in the temperature range of 375 to 4.2 K were collected by heating with a custom-built heater and cooling with a closed-cycle He refrigerator.

Magnetic properties were measured with a Quantum Design MPMS-XL SQUID spectrometer. Temperature dependence of the direct current (dc) magnetic susceptibility under various magnetic fields was measured over the temperature range 2−300 K under zero field cooling (ZFC) and field cooling (FC) conditions. The direct-current (dc) electrical resistance of the samples was measured in a four-probe configuration with a Quantum Design PPMS.

RESULTS AND DISCUSSION

Phase Identification and Structural Characterization of $Y_{0.9}Ba_{1.7}Ca_{2.4}Fe_5O_{13+\delta}$. Attempts to prepare stoichiometric $YBa_2Ca_2Fe_5O_{13}$ by the ceramic method, in analogy to other $REBa_2Ca_2Fe_5O_{13}$ (RE = Gd and Tb) oxides, led to the formation of the targeted perovskite-related phase with the presence of $BaFeO_3$ as the secondary phase. XEDS analysis revealed a composition of the main phase close to that of $Y_{0.9}Ba_{1.7}Ca_{2.4}Fe_5O_{13}$. Considering the chemical analysis, single-phase $Y_{0.9}Ba_{1.7}Ca_{2.4}Fe_5O_{13}$ with a dark-brown color was then prepared. The oxide presents a 10-fold perovskite superstructure with a $\sqrt{2}\,a_p x 2\sqrt{2}\,a_p x 10a_p$ unit cell that is ascribed to the layered ordering of the Y^{3+}, Ba^{2+}, and Ca^{2+} cations in combination with the layered ordering of the oxygen coordination polyhedra of the Fe atoms and the modulation of the $[FeO_4]$ tetrahedra within the (001) layers (Figure S1 Supporting Information). Details of the synthesis and characterization of the crystal structure of $Y_{0.9}Ba_{1.7}Ca_{2.4}Fe_5O_{13}$ have recently been reported by Martínez de Irujo Labalde et al.[24]

Ozone oxidation of $Y_{0.9}Ba_{1.7}Ca_{2.4}Fe_5O_{13}$ at 473 K gives a shiny black powder. The PXRD pattern and EDS analysis indicate single-phase formation. The PXRD pattern (Figure S2 Supporting Information) is well indexed as a single phase in the pseudo-tetragonal cell $\sqrt{2}\,a_p x \sqrt{2}\,a_p x 10a_p$. TGA (Figure S3 Supporting Information) shows an increase in the oxygen content up to 14.7(1) [δ = 1.7(1)], which is lower than that of the fully oxidized (stoichiometric) compound (δ = 2). The oxygen content has been determined assuming that after losing oxygen above 250 °C, the final compound is the stoichiometric $Y_{0.9}Ba_{1.7}Ca_{2.4}Fe_5O_{13}$. Given the oxygen content, a simple ionic model results in an average Fe valence state of 3.78+. The increase in the oxidation state after the ozone treatment seems to take place with the creation of holes in the oxygen band that presents Fe-3d and O-2p characters according to the EELS spectra at the O−K edges (Figure 1) and therefore reflects the high degree of hybridization between the O-2p and Fe-3d orbitals.

The SAED, HAADF-STEM, ABF-STEM, and EELS results (Figure 2) confirm the preservation of the 5-fold ordering of Y, Ba, and Ca and the 10-fold unit cell after oxidation. The SAED patterns were indexed according to the cubic perovskite. The cation ordering takes place in a Ca(Y)−Ba−Y(Ca)−Ba−Ca(Y)−Ca(Y) sequence. The Ca atoms are mainly located within two consecutive layers (with Ca being partially replaced by Y, see Table S1 Supporting Information); the Ba atoms are located in two layers of the unit cell separated by a layer that contains predominantly Y atoms with a significant proportion of Ca. The SAED pattern along the $[1{-}10]_p$ zone axis shows faint reflections leading to the 10-fold modulation associated with the Fe-coordination polyhedra.

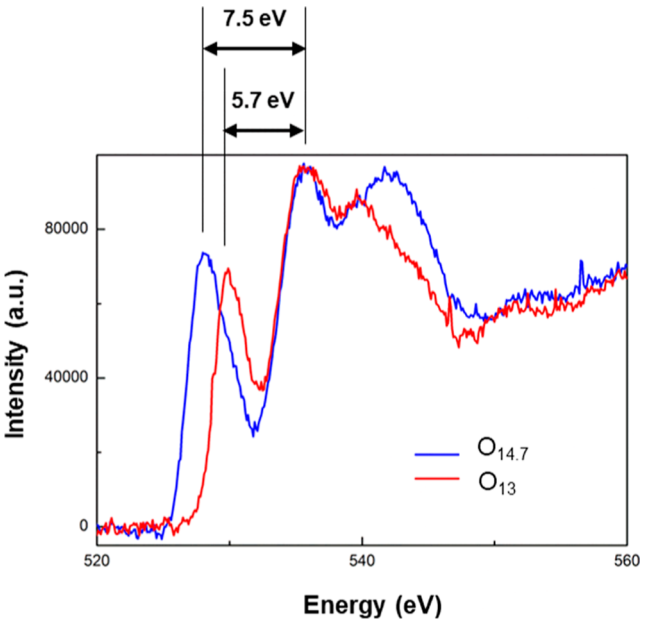

Figure 1. Comparative EELS spectra at the O−K edges of $Y_{0.9}Ba_{1.7}Ca_{2.4}Fe_5O_{13}$ (red) and $Y_{0.9}Ba_{1.7}Ca_{2.4}Fe_5O_{14.7}$ (blue).

On the contrary, the $G_p = \pm 1/4(1{-}10)_p$ reflections detected in the SAED patterns of $Y_{0.9}Ba_{1.7}Ca_{2.4}Fe_5O_{13}$ along the $[001]_p$ zone axis, which are associated with the ordering of the FeO_4 tetrahedra within the $(00l)_p$ planes and lead to the $2\sqrt{2}\,a_p$ periodicity, are not detected in the compound after oxidation due to the resulting occupation of oxygen positions. Therefore, the cation ordering of the average crystal structure of the pristine $Y_{0.9}Ba_{1.7}Ca_{2.4}Fe_5O_{13}$ seems to be maintained after oxidation in the $\sqrt{2}\,a_p x \sqrt{2}\,a_p x 10a_p$ unit cell. However, the SXRD pattern at RT (Figure 3) shows the splitting of some reflections, which can only be indexed, according to the Le Bail fitting of the data, in a monoclinic symmetry with a = 5.4520(1) Å, b = 5.4526(1) Å, and c = 38.6168(5) Å lattice parameters and β = 89.890(1) angle, despite observing a cell metrically tetragonal (*pseudo*-tetragonal) from SAED. Close inspection of the SAED and SXRD patterns concludes extinction conditions (00l: $l = 2n$; h00: $h = 2n$; h0l: $h + l = 2n$+1 or $h + k + l = 2n + 1$), which can be associated with an I centering or an n plane. Starting from a structural model in the high symmetry $I4/mmm$ space group and through the analysis of group−subgroup relationships with the assistance of the ISODISTORT software package,[26,27] we have constructed different structural models in the three monoclinic space groups that accomplish the extinction conditions found above: the primitive $P2_1/n$, the body-centered $I2/m$, and the Im space groups. Goodness of fitting of the Rietveld refinement discards only the Im space group with nonsignificant differences between the two others. However, complementary micro-diffraction analysis (Figure 2b,c) suggests that the only possible space group is $P2_1/n$ since the similarity between the first-order Laue zone (FOLZ) and the zero-order Laue zone (ZOLZ) clearly indicates a P centering.[28] The structural

https://doi.org/10.1021/acs.chemmater.4c00552
Chem. Mater. 2024, 36, 5184−5191

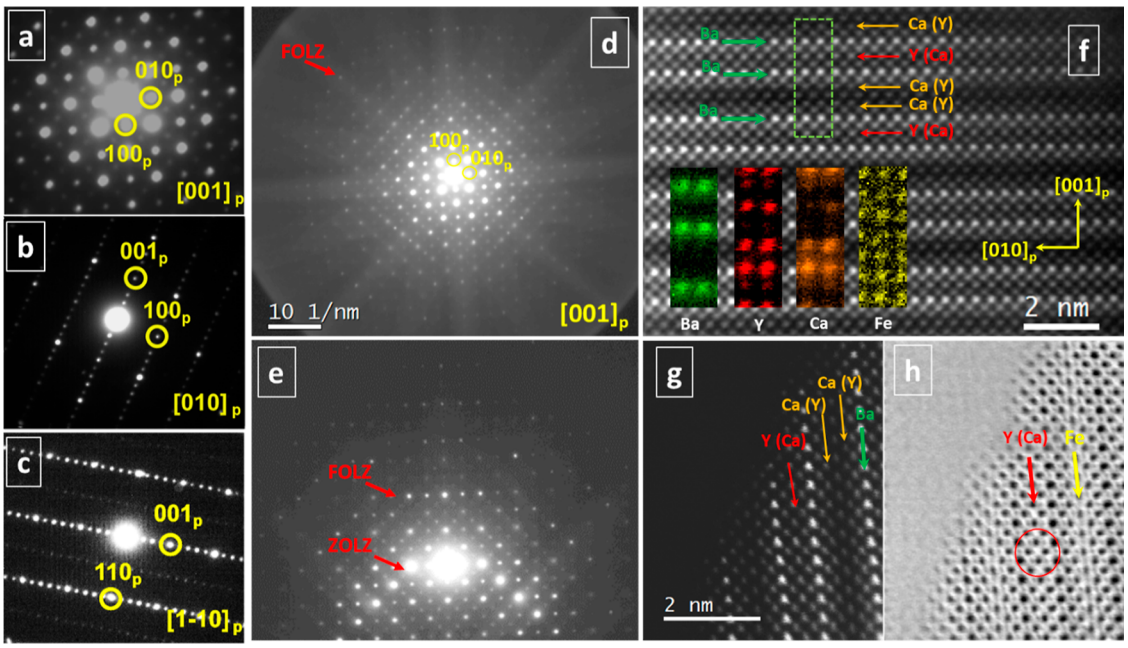

Figure 2. SAED patters along the (a) $[001]_p$, (b) $[010]_p$, and (c) $[1{-}10]_p$ zone axes. The patterns were indexed according to the cubic perovskite. Equivalency of the reflections with the diagonal $\sqrt{2}a_p \times \sqrt{2}a_p \times 10a_p$ cell: $[110]_p = [100]_d$; $[001]_p = [001]_d$. (d) Electron microdiffraction pattern along the $[001]_p$ zone axis, where the FOLZ is arrowed. The $G_p \pm 1/2(010)_p$ and $G_p \pm 1/2(100)$reflections are due to multiple diffraction. (e) Tilted diffraction pattern where the FOLZ periodicity is more clearly observed: the same ZOLZ and FOLZ periodicity without displacements is compatible with a primitive cell. (f) HAADF−STEM image of a $Y_{0.9}Ba_{1.7}Ca_{2.4}Fe_5O_{14.7}$ crystal along the $[100]_p$ zone axis. EELS maps from the area squared in the image. The EELS edges employed for each map are the following: Ba-$M_{4,5}$, Y-$L_{2,3}$, Ca-$L_{2,3}$, and Fe$L_{2,3}$. (g) HAADF−STEM and corresponding (h) ABF−STEM images of a $Y_{0.9}Ba_{1.7}Ca_{2.4}Fe_5O_{14.7}$ crystal along the $[010]_p$ zone axis.

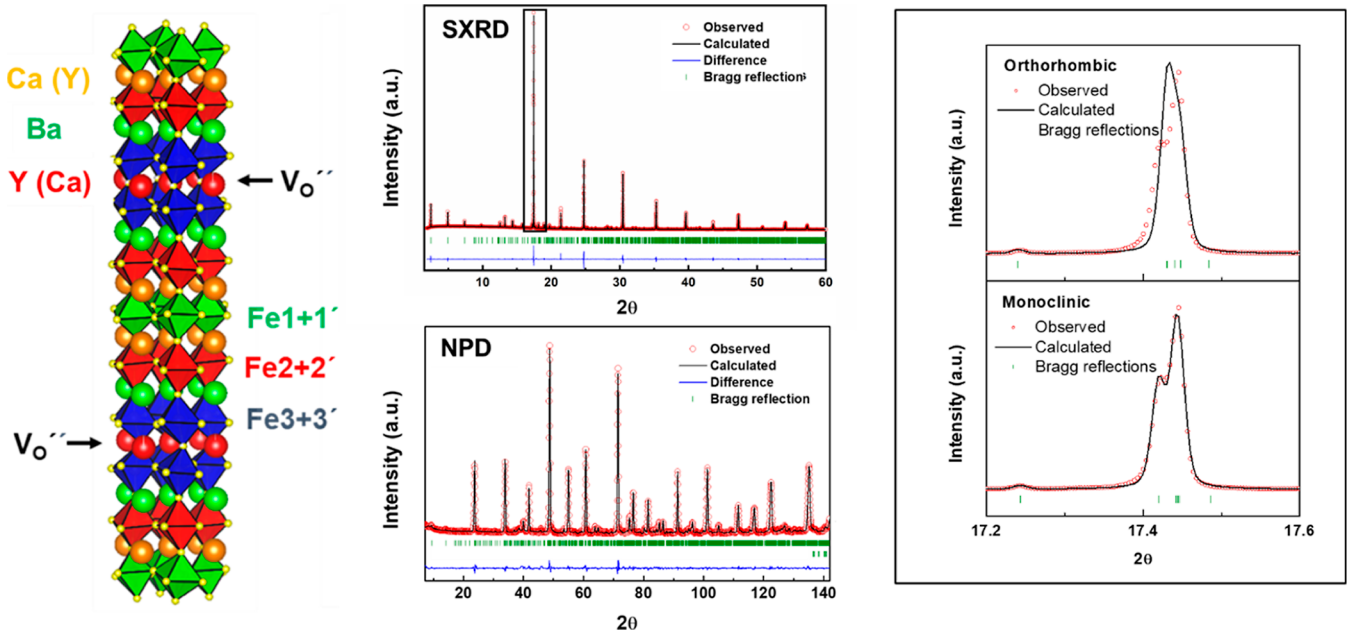

Figure 3. Graphic representation of the crystal structure of $Y_{0.9}Ba_{1.7}Ca_{2.4}Fe_5O_{14.7}$ (left). Anion vacancies are located within the Y(Ca) planes. Experimental and calculated SXRD (middle top) and NPD (middle bottom) patterns at RT of $Y_{0.9}Ba_{1.7}Ca_{2.4}Fe_5O_{14.7}$. Selected 2θ region of the SXRD pattern (right).

model has been used to refine the SXRD and ND data taken at RT. Figure 3 shows the fitted NPD pattern. The calculated cell parameters, crystallographic positions, and fitting values given from the refinement against ND are collected in Table S1 Supporting Information. Table S2 Supporting Information contains the Fe−O distances and the BVS values for the Fe cations within the structure. The crystal structure of $Y_{0.9}Ba_{1.7}Ca_{2.4}Fe_5O_{14.7}$ obtained from the Rietveld refinement is also depicted in Figure 2. The oxygen content agrees with that determined from the TGA experiments. The results show that the topochemically incorporated oxygen in $Y_{0.9}Ba_{1.7}Ca_{2.4}Fe_5O_{14.7}$ is accommodated within the crystal structure, resulting in octahedral coordination of the Fe atoms with anion vacancies located at the Y(Ca) planes (30%

https://doi.org/10.1021/acs.chemmater.4c00552
Chem. Mater. 2024, 36, 5184−5191

of oxygen vacancies according to the determined oxygen content). The accommodation of the extra oxygen in $Y_{0.9}Ba_{1.7}Ca_{2.4}Fe_5O_{14.7}$ induces a phase transformation from an orthorhombic to a monoclinic symmetry. The resulting $P2_1/n$ space group can be explained by the tilting and distortion of octahedra, mainly the ones formed between the Ca(Y) layers, which need to be extremely distorted to be accommodated within the structure.

As a result, three different Fe sites must be considered: Fe1 located between the two consecutive Ca(Y) layers, Fe2 between a Ba-layer and a Ca(Y) one, and Fe3 located between the Ba and Y(Ca) layers. These results are in agreement with the ABF images. Figure 2h depicts the ABF-STEM image of a crystal of $Y_{0.9}Ba_{1.7}Ca_{2.4}Fe_5O_{14.7}$ along the $[010]_p$ zone axis. The image reveals the low intensity of two positions of columns of oxygen atoms around the Y(Ca) columns (the red circle marks the one), indicating the location of the anion vacancies. Besides, the different intensity of the oxygen−Fe layers between the two consecutive Ca(Y) layers (indicated by a yellow arrow) announces the different oxygen arrangements around these Fe atoms due to the huge distortion of their coordination polyhedra.

In addition, a set of SXRD data were collected at different temperatures. Variations of cell parameters as a function of temperature extracted from the Lebail fitting of the corresponding SXRD data are depicted in Figure S4 Supporting Information. No less or extra reflections were observed in the SXRD patterns up to 300 K, which indicates that the $P2_1/n$ space group is preserved. However, the SXRD patterns collected at 400 and 450 K show a gradual merge of reflections resulting from a change in the lattice parameters and of the β angle getting closer to 90°, which indicates that the phase gradually evolves toward an orthorhombic symmetry upon heating above 300 K due to the loss of the topochemically inserted oxygen. The temperature of the complete phase transformation seems to be higher than 450 K as oxygen release starts close to 500 K according to TGA.

Charge Evolution of $Y_{0.9}Ba_{1.7}Ca_{2.4}Fe_5O_{14.7}$. The Fe charge state and its possible thermal evolution have been followed by means of Mössbauer spectroscopy in the temperature range between 370 and 5 K (Figure S5 Supporting Information). Fitting results of the spectra collected at 370, 300, and 150 K are shown in Figure 4 and Table 1.

The three spectra are well fitted with a doublet component with isomer shifts consistent with Fe in the high oxidation state (3.78+), in accordance with the BVS values above 3+ in all the Fe crystallographic sites at 300 K (Table 1). In addition, the three different quadrupole splitting values agree with the existence of three different environments of the Fe atoms, as determined by the refinement of the crystal structure. Therefore, CD does not seem to occur in the range of temperatures between 370 and 150 K, but a mixed valence state with Fe in the 3.78+ oxidation state is maintained. Fitting of the spectrum at 100 K (Figure S6 Supporting Information) is not good enough because the sextet magnetic splitting is small. However, it shows that magnetic ordering is already formed at 100 K. On the contrary, both the spectra at 50 and 5 K (Figure 5 and Table 2) consist of three components with three magnetic sextets, two of them with similar integrated intensity and another with half of the integrated intensity.

The IS of about 0.4 mm s^{-1} agrees with Fe^{3+} with oxygen-octahedra coordination. The IS values of 0.05 mm s^{-1} and 0.07 mm s^{-1} of the spectrum collected at 50 K seem to be closer to

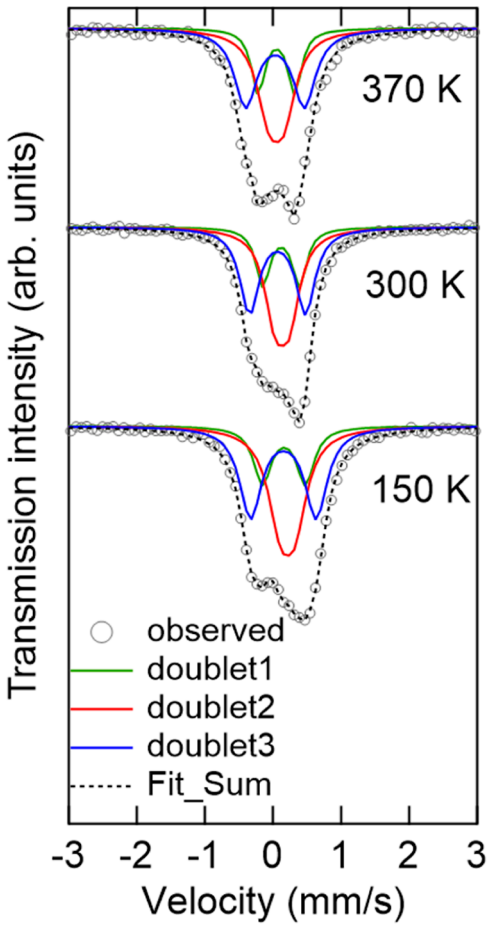

Figure 4. Mössbauer spectra of $Y_{0.9}Ba_{1.7}Ca_{2.4}Fe_5O_{14.7}$ at 370, 300, and 150 K. The circles show experimental data and the lines show Lorentzian fits.

Table 1. Parameters for the Fitting of the Mössbauer spectra of $Y_{0.9}Ba_{1.7}Ca_{2.4}Fe_5O_{14.7}$ at 370, 300, and 150 K

	component	IS (mm/s)	QS (mm/s)	%
370 K	**Fe1**	0.0504	0.5356	20
	Fe2	0.0504	0.2231	40
	Fe3	0.0288	0.8623	40
300 K	**Fe1**	0.1199	0.5379	20
	Fe3	0.1334	0.2098	40
	Fe3	0.0662	0.8218	40
150 K	**Fe1**	0.1608	0.6325	20
	Fe2	0.2138	0.2188	40
	Fe3	0.1524	0.9635	40

Fe in the $(4+\delta)+$ oxidation state, and the IS values of 0.105 and −0.007 mm s^{-1} in the spectrum collected at 5 K can be assigned to the $(4+\delta)+$ oxidation states. Therefore, the results indicate a gradual CD below 150 K that consists of 5 $Fe^{3.8+} \rightarrow 2\ Fe^{3+} + 3\ Fe^{(4+\delta)+}$.

Considering the Mössbauer results, in combination with the refinement of the crystal structure, we suggest a possible model of charge distribution within the different Fe layers (Figure 6): the $Fe^{(4+\delta)+}$ atoms located between two layers of Ca(Y), with high distorted coordination polyhedra, and between one layer of Ba and one layer of Y(Ca) since these Fe atoms increase the oxygen coordination environment after the topotactic oxygen insertion; the Fe^{3+} located between one layer of Ba and one

https://doi.org/10.1021/acs.chemmater.4c00552
Chem. Mater. 2024, 36, 5184−5191

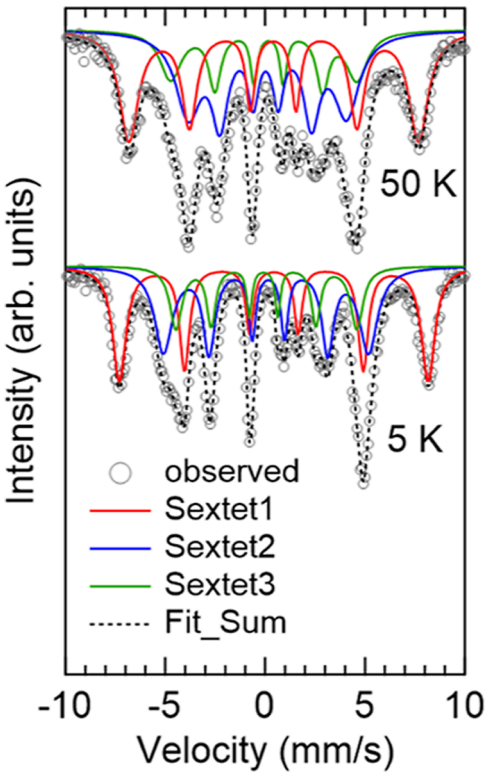

Figure 5. Mössbauer spectra of $Y_{0.9}Ba_{1.7}Ca_{2.4}Fe_5O_{14.7}$ at 50 and 5 K. The circles show experimental data and the lines show Lorentzian fits.

Table 2. Parameters for the Fitting of the RT Mössbauer Spectra of $Y_{0.9}Ba_{1.7}Ca_{2.4}Fe_5O_{14.7}$ at 50 and 5 K

	component	IS (mm/s)	QS (mm/s)	HF (T)	%
50 K	**Fe1**	0.055	−0.2508	28.7	20
	Fe2	0.4198	0.0287	45.0	40
	Fe3	0.0732	0.0891	24.5	40
5 K	**Fe1**	−0.0071	0.1403	28.1	20
	Fe2	0.4364	−0.0089	47.9	40
	Fe3	0.1048	−0.1222	31.8	40

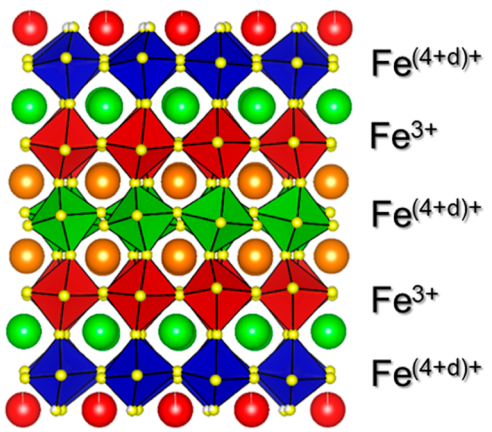

Figure 6. Proposed CO model of $Y_{0.9}Ba_{1.7}Ca_{2.4}Fe_5O_{14.7}$.

layer of Ca(Y) since the coordination polyhedra around these Fe-atoms is not significantly modified with the oxidation of the compound.

Magnetic and Electric Characterization of $Y_{0.9}Ba_{1.7}Ca_{2.4}Fe_5O_{14.7}$. Zero-field cooled (ZFC) and field cooled (FC) magnetization data of $Y_{0.9}Ba_{1.7}Ca_{2.4}Fe_5O_{14.7}$ were collected between 5 and 300 K in an applied field of 100 Oe (Figure 7a). ZFC and FC curves strongly diverge below 125 K,

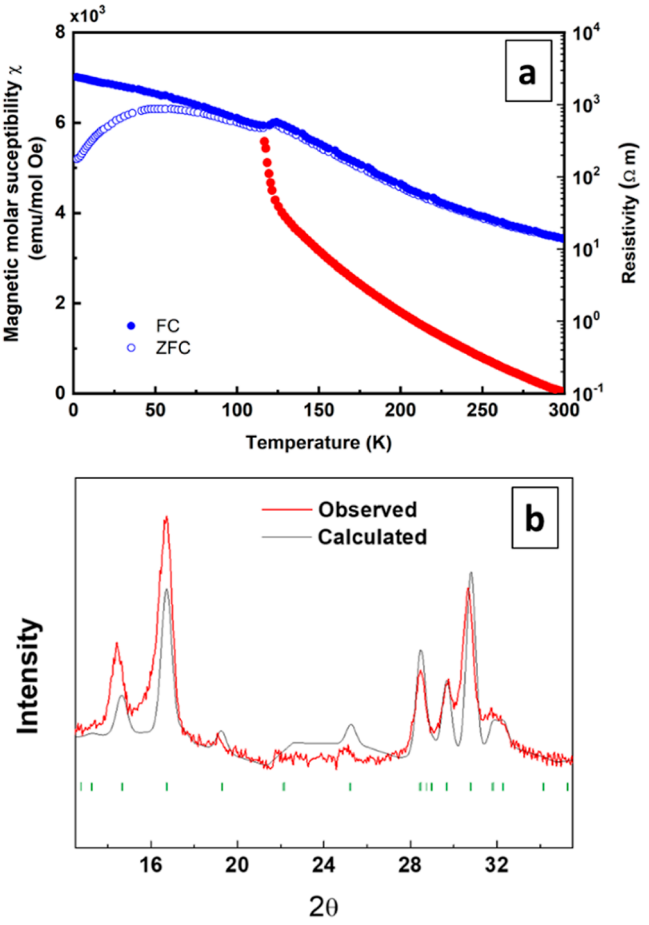

Figure 7. (a) Temperature-dependence of magnetic susceptibility and resistivity of $Y_{0.9}Ba_{1.7}Ca_{2.4}Fe_5O_{14.7}$. (b) Purely magnetic diffraction intensity of $Y_{0.9}Ba_{1.7}Ca_{2.4}Fe_5O_{14.7}$ created by the subtraction of the NPD pattern recorded at 150 K from the one recorded at 2 K. The tick marks correspond to the position of magnetic Bragg peaks using $k_1 = [1/2, 0, 0]$.

indicating a magnetic phase transition at that temperature. Data in the range 150 K < T < 300 K do not obey the Curie–Weiss law, suggesting that magnetic interactions also occur within this temperature range. Magnetization data collected at 300 K exhibit a linear field dependence characteristic of paramagnetic behavior. The electric resistance of $Y_{0.9}Ba_{1.7}Ca_{2.4}Fe_5O_{14.7}$ was measured between 5 and 300 K (Figure 6a). The oxide shows semiconducting behavior in the whole temperature range with a marked change in the trend below 125 K. Therefore, both the magnetic and electric transition occur at 125 K.

NPD patterns collected between 300 and 2 K show extra reflections below 140 K associated with long-range magnetic ordering. It is worth mentioning that bumps are observed even close to RT, which indicates that weak short-range magnetic ordering remains above the magnetic transition as it is inferred in the ZFC-FC curves, but they are not detected by Mössbauer spectroscopy due to the short-range character.

The magnetic behavior of $Y_{0.9}Ba_{1.7}Ca_{2.4}Fe_5O_{14.7}$ can be associated with systems with certain bidimensional charac-

https://doi.org/10.1021/acs.chemmater.4c00552
Chem. Mater. 2024, 36, 5184−5191

ters.[23,29,30] Figure 7b shows the difference between the NPD patterns at 150 and 2 K to better visualize the magnetic reflections. The magnetic reflections can be indexed by a propagation vector $k_1 = [1/2, 0, 0]$, producing a magnetic unit cell $2\sqrt{2}\,a_p x \sqrt{2}\,a_p x 10 a_p$. However, a more detailed inspection (Figure 7b) reveals that the reflections at 2θ 14.6 and 30.8° are slightly shifted from the position calculated using k_1. A second incommensurate propagation vector $k_2 = [\delta, 0, 0]$ could be a better choice to index this second set of reflections. However, building a magnetic model at this point is very challenging because different spin alignments between the different Fe charge states within the structure can be considered according to the CO model proposed.

Thus, according to the Goodenough Kanamori rules, superexchange AFM interactions are expected between Fe atoms in the same layer, while the 3D-interactions seem not to be well established since the intercalation of the $Fe^{(4+\delta)+}$ layers between the Fe^{3+} layers might create magnetic disruptions that probably explain the coexistence of two propagation vectors, with a second one incommensurate in order to accommodate helical magnetic components.

CONCLUSIONS

Oxidation of $Y_{0.9}Ba_{1.7}Ca_{2.4}Fe_5O_{13}$ under an ozone atmosphere results in the topochemical insertion of oxygen in particular sites of the crystal structure. The Fe^{3+} cations in $Y_{0.9}Ba_{1.7}Ca_{2.4}Fe_5O_{13}$ present three different oxygen-coordination environments (octahedral, squared pyramidal, and tetrahedral) in such a way that the extra oxygen after oxidation is accommodated in $Y_{0.9}Ba_{1.7}Ca_{2.4}Fe_5O_{14.7}$ by filling the nonoccupied positions of the anion sublattice, leading to the formation of highly distorted octahedra. The average oxidation state of Fe is 3.78+, and the anion vacancies are mainly located at the Y(Ca)-layers. The electronic instability of MV-$Y_{0.9}Ba_{1.7}Ca_{2.4}Fe_5O_{14.7}$ is relieved by a CD described as 5 $Fe^{3.8+} \rightarrow 2\ Fe^{3+} + 3\ Fe^{(4+\delta)+}$ according to the Mössbauer spectra below 50 K. A layered model for the accommodation of Fe^{3+} and $Fe^{(4+\delta)+}$, in agreement with the modifications of the layered crystal structure after oxidation, is suggested. The MV/CD transition seems to take place below 125 K, accompanied by a smooth magnetic and electric transition. Superexchange antiferromagnetic interactions, mainly between Fe^{3+} cations in the plane, probably occur, but only 2D-magnetic ordering seems to be established due to the intercalation of the $Fe^{(4+\delta)+}$ layers.

ASSOCIATED CONTENT

Supporting Information

The Supporting Information is available free of charge at https://pubs.acs.org/doi/10.1021/acs.chemmater.4c00552.

Crystal structure and profile matching against PXRD of $Y_{0.9}Ba_{1.7}Ca_{2.4}Fe_5O_{13}$, TGA results, EELS spectra at the O−K O−K edge, refined crystal structure parameters, Fe−O distances at 300 K, and lattice parameter variation between 80 and 450 K of $Y_{0.9}Ba_{1.7}Ca_{2.4}Fe_5O_{14.7}$ (PDF)

AUTHOR INFORMATION

Corresponding Authors

Yuichi Shimakawa − *Institute for Chemical Research, Kyoto University, Uji, Kyoto 611-0011, Japan;* orcid.org/0000-0003-1019-2512; Phone: (+81) 774 38 3110; Email: shimak@scl.kyoto-u.ac.jp

Susana García-Martín − *Departamento de Química Inorgánica I, Facultad de Ciencias Químicas, Universidad Complutense, Madrid 28040, Spain;* orcid.org/0000-0003-0729-4892; Phone: (+34) 91 394 4214; Email: sgmartin@ucm.es

Authors

Xabier Martínez de Irujo-Labalde − *Departamento de Química Inorgánica I, Facultad de Ciencias Químicas, Universidad Complutense, Madrid 28040, Spain; Institute of Inorganic and Analytical Chemistry, University of Münster, Münster 48149, Germany; Institute for Chemical Research, Kyoto University, Uji, Kyoto 611-0011, Japan*

Masato Goto − *Institute for Chemical Research, Kyoto University, Uji, Kyoto 611-0011, Japan;* orcid.org/0000-0002-8198-7622

Esteban Urones-Garrote − *Departamento de Química Inorgánica I, Facultad de Ciencias Químicas, Universidad Complutense, Madrid 28040, Spain;* orcid.org/0000-0002-4745-2755

Ulises Amador − *Departamento de Química y Bioquímica, Urbanización Montepríncipe, Facultad de Farmacia, Universidad San Pablo-CEU, CEU Universities, Boadilla del Monte, Madrid E-28668, Spain;* orcid.org/0000-0002-4412-2419

Clemens Ritter − *Institut Laue-Langevin, Grenoble, Cedex 9 BP 156-38042, France*

Midori Amano-Patino − *Institute for Chemical Research, Kyoto University, Uji, Kyoto 611-0011, Japan*

Complete contact information is available at: https://pubs.acs.org/10.1021/acs.chemmater.4c00552

Notes

The authors declare no competing financial interest.

ACKNOWLEDGMENTS

This work has been supported by the Spanish MCIN/AEI/10.13039/501100011033 with the projects PID2022-139039OB-C22, PID2019-106662RB-C44, and PID2019-106662RB-C41 and by "NextGenerationEU"/PRTR with the project TED2021-130452B−C21. We also thank ILL for the allocation of beam time (experiment codes 5-21-1116; doi: 10.5291/ILL-DATA.5-21-1116). X.M. d. I.-L. thanks the MECD for the grant FPU014/05971. This work was partly supported by Grants-in-Aids for Scientific Research (Nos. 20H00397, 23H05457, and 23K13814) from MEXT and by AdCORP (No. JPMJKB2304) and ASPIRE (JPMJAP2314) programs from JST, Japan, by the International Collaborative Research Program of Institute for Chemical Research in Kyoto University, and by JSPS Core-to-Core Program(A) Advanced Research Networks.

REFERENCES

(1) Goodenough, J. B. Perspective on Engineering Transition-Metal Oxides. *Chem. Mater.* **2014**, *26*, 820−829.

(2) Verwey, E. J. Electronic Conduction of Magnetite (Fe3O4) and its Transition Point at Low Temperatures. *Nature* **1939**, *144*, 327−328.

(3) Imada, M.; Fujimori, A.; Tokura, Y. Metal-insulator transitions. *Rev. Mod. Phys.* **1998**, *70*, 1039−1263.

(4) Zhang, N.; Chai, Y. Lattice oxygen redox chemistry in solid-state electrocatalysts for water oxidation. *Energy Environ. Sci.* **2021**, *14*, 4647−4671.
(5) Rao, C. N. R.; Raveau, B. *Colossal Magnetoresistance, Charge Ordering and Related Properties of Manganese Oxides*; World Scientific, 1998.
(6) Hosaka, Y.; Denis Romero, F.; Ichikawa, N.; Saito, T.; Shimakawa, Y. Successive Charge Transitions of Unusually High-Valence $Fe^{3.5+}$: Charge Disproportionation and Intermetallic Charge-Transfer. *Angew. Chem., Int. Ed.* **2017**, *56*, 4243−4246.
(7) Denis Romero, F.; Shimakawa, Y. Charge transitions in perovskite oxides containing unusually high-valent Fe. *Chem. Commun.* **2019**, *55*, 3690−3696.
(8) MacChesney, J. B.; Sherwood, R. C.; Potter, J. F. Electric and Magnetic Properties of the Strontium Ferrates. *J. Chem. Phys.* **1965**, *43*, 1907−1913.
(9) Bocquet, A. E.; Fujimori, A.; Mizokawa, T.; Saitoh, T.; Namatame, H.; Suga, S.; Kimizuka, N.; Takeda, Y.; Takano, M. Electronic Structure of $SrFe^{4+}O_3$ and Related Fe Perovskite Oxides. *Phys. Rev. B* **1992**, *45*, 1561−1570.
(10) Takano, M.; Nakanishi, N.; Takeda, Y.; Naka, S.; Takada, T. Charge disproportionation in $CaFeO_3$ studied with the Mössbauer effect. *Mater. Res. Bull.* **1977**, *12*, 923−928.
(11) Woodward, P.; Cox, D.; Moshopoulou, E.; Sleight, A. W.; Morimoto, S. Structural studies of charge disproportionation and magnetic order in $CaFeO_3$. *Phys. Rev. B Condens. Matter. Mater. Phys.* **2000**, *62*, 844−855.
(12) Takeda, T.; Kanno, R.; Kawamoto, Y.; Takano, M.; Kawasaki, S.; Kamiyama, T.; Izumi, F. Metal-semiconductor transition, charge disproportionation, and low-temperature structure of $Ca_{1-x}Sr_xFeO3$ synthesized under high-oxygen pressure. *Solid State Sci.* **2000**, *2*, 673−687.
(13) Takano, M.; Kawachi, J.; Nakanishi, N.; Takeda, Y. Valence state of the Fe ions in $Sr_{1-y}La_yFeO_3$. *J. Solid State Chem.* **1981**, *39*, 75−84.
(14) Woodward, P. M.; Karen, P. Mixed Valence in $YBa_2Fe_2O_5$. *Inorg. Chem.* **2003**, *42* (4), 1121−1129.
(15) Guo, H.; Hosaka, Y.; Romero, F. D.; Saito, T.; Ichikawa, N.; Shimakawa, Y. Two Charge Ordering Patterns in the Topochemically Synthesized Layer-Structured Perovskite LaCa 2 Fe 3 O 9 with Unusually High Valence Fe $^{3.67+}$. *Inorg. Chem.* **2017**, *56*, 3695−3701.
(16) Arevalo-Lopez, A. M.; Hosaka, Y.; Guo, H.; Denis Romero, F.; Saito, T.; Attfield, J. P.; Shimakawa, Y. Spin order in the charge disproportionated phases of the A-site layer ordered triple perovskite $LaCa_2Fe_3O_9$. *Phys. Rev. B* **2018**, *97*, 024421.
(17) Iihoshi, M.; Goto, M.; Kosugi, Y.; Shimakawa, Y. Cascade Charge Transitions of Unusually High and Mixed Valence $Fe^{3.5+}$ in the A-Site Layer-Ordered Double Perovskite $SmBaFe_2O_6$. *J. Am. Chem. Soc.* **2023**, *145*, 10756−10762.
(18) Li, J. Q.; Matsui, Y.; Park, S. K.; Tokura, Y. Charge ordered states in $La_{1-x}Sr_xFeO_3$. *Phys. Rev. Lett.* **1997**, *79*, 297−300.
(19) Hodges, J.; Short, S.; Jorgensen, J. D.; Xiong, X.; Dabrowski, B.; Mini, S. M.; Kimball, C. W. Evolution of Oxygen-Vacancy Ordered Crystal Structures in the Perovskite Series $Sr_nFe_nO3_{n-1}$ (n = 2, 4, 8, and ∞), and the Relationship to Electronic and Magnetic Properties. *J. Solid State Chem.* **2000**, *151*, 190−209.
(20) Lebon, A.; Adler, P.; Bernhard, C.; Boris, A. V.; Pimenov, A. V.; Maljuk, A.; Lin, C. T.; Ulrich, C.; Keimer, B. Magnetism, Charge Order, and Giant Magnetoresistance in $SrFeO_{3-\delta}$ Single Crystals. *Phys. Rev. Lett.* **2004**, *92*, 037202.
(21) Reehuis, M.; Ulrich, C.; Maljuk, A.; Niedermayer, Ch.; Ouladdiaf, B.; Hoser, A.; Hofmann, T.; Keimer, B. Neutron diffraction study of spin and charge ordering in $SrFeO_{3-\delta}$. *Phys. Rev. B Condens Matter Mater. Phys.* **2012**, *85*, 184109.
(22) Marín-Gamero, R.; Martínez de Irujo-Labalde, X.; Urones-Garrote, E.; García-Martín, S. Structural Ordering Supremacy on the Oxygen Reduction Reaction of Layered Iron-Perovskites. *Inorg. Chem.* **2020**, *59*, 5529−5537.
(23) Martínez de Irujo-Labalde, X. M.; Amador, U.; Ritter, C.; Goto, M.; Patino, M. A.; Shimakawa, Y.; García-Martín, S. 3D to 2D Magnetic Ordering of Fe^{3+}Oxides Induced by Their Layered Perovskite Structure. *Inorg. Chem.* **2021**, *60*, 8027−8034.
(24) Martínez de Irujo-Labalde, X. M.; Urones Garrote, E.; García Martín, S. Revisiting the crystal structure of the $Y_{0.9}Ba_{1.7}Ca_{2.4}Fe_5O_{13}$ layered-type perovskite: new interplay of the cation ordering & the modulation of the anion sublattice. *Solid State Sci.* **2024**, *151*, 107516.
(25) Rodriguez-Carvajal, J. Structural Analysis from Powder Diffraction Data The Rietveld Method.Ec. Themat. *Cristallogr. Neutrons* **1997**, *418*, 73−95.
(26) Campbell, B. J.; Stokes, H. T.; Tanner, D. E.; Hatch, D. M. ISODISPLACE: A Web-Based Tool for Exploring Structural Distortions. *J. Appl. Crystallogr.* **2006**, *39* (4), 607−614.
(27) ISOTROPY Software Suite. https://stokes.byu.edu/iso/isotropy.php (accessed April 9, 2024).
(28) Morniroli, J. P.; Steeds, J. W. Microdiffraction as a tool for crystal structure identification and determination. *Ultramicroscopy* **1992**, *45*, 219−239.
(29) Ramezanipour, F.; Cowie, B.; Derakhshan, S.; Greedan, J. E.; Cranswick, L. M. D. Crystal and magnetic structures of the brownmillerite compound $Ca_2Fe_{1.039(8)}Mn_{0.962(8)}O_5$. *J. Solid State Chem.* **2009**, *182*, 153−159.
(30) Butera, A.; Fainstein, A.; Winkler, E.; Tallon, J. Ferromagneticcorrelations and mixed Ru valence in the magnetic superconductor $RuSr_2(Eu,Gd)Cu_2O_8$. *Phys. Rev. B* **2001**, *63*, 054442.

https://doi.org/10.1021/acs.chemmater.4c00552
Chem. Mater. 2024, 36, 5184−5191